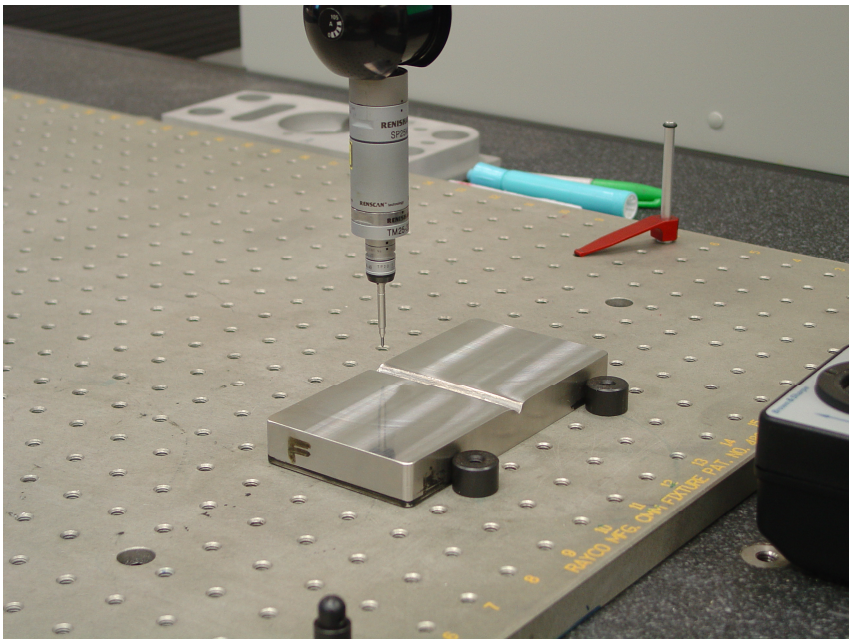

Figure 2-5. CMM Scan on Alloy 22 Plate Using a 60°-Angle Touch Probe

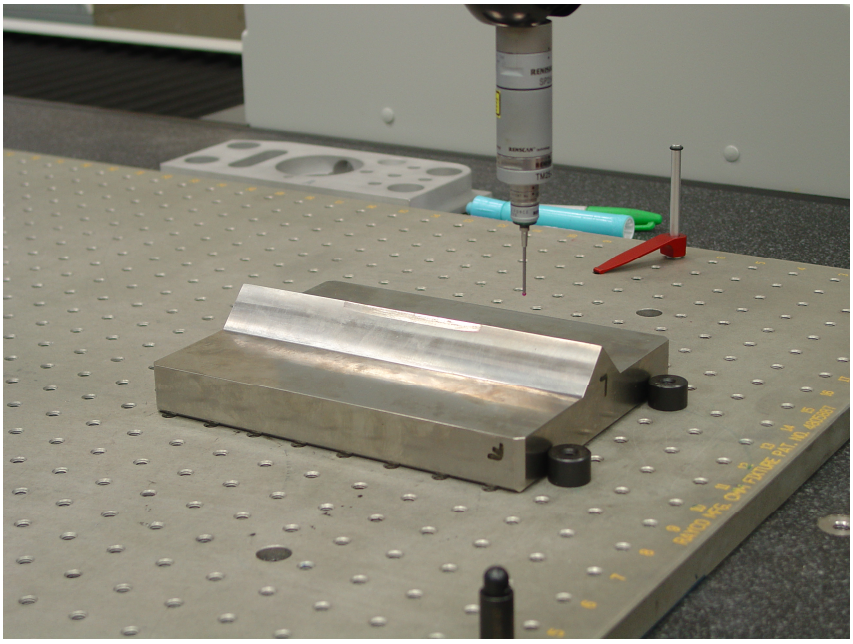

Figure 2-6. CMM Scan on Titanium Grade 5 Plate Using a 2-mm [0.079-in] Ruby Ball Touch Probe

2.3 Material Properties

The mechanical properties of Titanium Grade 24 and Alloy 22 used in the numerical plane strain model (Ibarra, et al., 2007b) are presented in Tables 2-1 and 2-2 for a temperature of 150 °C [302 °F]. The data for Titanium Grade 24 correspond to those of the surrogate material Titanium Grade 5, which exhibits similar mechanical characteristics (Ankem and Wilt, 2006). As observed in Table 2-1, Alloy 22 has a larger Young's modulus and density than the titanium alloy. Also, the yield stress, ultimate tensile strength (peak strength), and strain at ultimate tensile strength data presented in Table 2-2 indicate that Alloy 22 has a smaller elastic strength, but is a much more ductile material than Titanium Grade 24.

The material properties for the as-received material used in the experiment are presented in Table 2-3 for room temperature. For the titanium material, the yield stress and ultimate tensile strength experiment data are larger than those presented in Table 2-2, which are obtained from standards for a higher temperature. For Alloy 22, the as-received material properties at room temperature (Table 2-3) are close to the results obtained from tensile tests at 150 °C [302 °F] (Table 2-3). The effect of temperature on the material properties presented in Figure 2-7 indicates that Alloy 22 properties are not significantly affected as the temperature increases from room temperature to 150 °C [302 °F]. For Titanium Grade 24, this temperature increase affects mainly the yield stress and the ultimate tensile strength.

Table 2-1. Material Properties at 150 °C [302 °F]

Material	Density, tonne/m^3 [lb/in^3]	Young's Modulus, GPa [ksi]	Poisson's Ratio
Titanium Grade 24	4.512 [0.163]*	107.2 [15,500]†	0.32‡
Alloy 22	8.691 [0.314]§	179.9 [26,100]‖	0.32§

*ASME International. "ASME International Boiler and Pressure Vessel Code." Table NF–2, Typical Physical Properties of Nonferrous Materials (Unalloyed Titanium). New York City, New York: ASME International. 2004.
†U.S. Department of Defense. "Military Handbook: Metallic Materials and Elements for Aerospace Vehicle Structures." Figure 5.4.1.1.4, Effect of Temperature on the Tensile and Compressive Moduli of Annealed Ti-6Al-4V Alloy Sheet and Bar. MIL–HDBK–5H. Washington, DC: U.S. Department of Defense. 1998.
‡ASME International. "ASME International Boiler and Pressure Vessel Code." Table NF–1, Typical Mechanical Properties of Materials (Unalloyed Titanium). New York City, New York: ASME International. 2004.
§ASTM International. "Standard Specification for Low-Carbon Nickel-Molybdenum-Tungsten Alloy Plate, Sheet, and Strip." New York City, New York: ASTM International. 1998.
‖Center for Nuclear Waste Regulatory Analyses Experimental Data. From Ibarra, L., T. Wilt, G. Ofoegbu, R. Kazban, F. Ferrante, and A. Chowdhury. "Drip Shield–Waste Package Mechanical Interaction." San Antonio, Texas: Center for Nuclear Waste Regulatory Analyses. 2007.

Table 2-2. True Stresses and Strains for Titanium and Alloy 22 Materials at 150 °C [302 °F]			
Material	**Yield Stress, MPa [ksi]**	**Ultimate Tensile Strength, MPa [ksi]**	**Strain at Ultimate Tensile Strength, Percent**
Titanium Grade 24	658.1 [95.4]*	804.4 [116.7]*	6.60*
Alloy 22	257.7 [37.4]†	954.1 [138.5]†	33.63‡
Alloy 22§ (experimental data)	279.9 [40.6] §	1,216.2 [176.5]§	55.46§

*U.S. Department of Defense. "Military Handbook: Metallic Materials and Elements for Aerospace Vehicle Structures." Figure 5.4.1.1.4, Effect of Temperature on the Tensile and Compressive Moduli of Annealed Ti-6Al-4V Alloy Sheet and Bar. MIL–HDBK–5H. Washington, DC: U.S. Department of Defense. 1998.
†ASME International. "ASME International Boiler and Pressure Vessel Code." Section II, Part D, Tables U and Y–1. New York City, New York: ASME International. 2004.
‡_____. "ASME International Boiler and Pressure Vessel Code." Section II, Part B, Tables 1 and 4. New York City, New York: ASME International. 2004.
§Ibarra, L., T. Wilt, G. Ofoegbu, R. Kazban, F. Ferrante, and A. Chowdhury. "Drip Shield–Waste Package Mechanical Interaction." San Antonio, Texas: Center for Nuclear Waste Regulatory Analyses. 2007.

Table 2-3. True Stresses and Strains for Titanium and Alloy 22 Materials at Room Temperature (Properties of As-Delivered Material)			
Material	**Yield Stress, MPa [ksi]**	**Ultimate Tensile Strength, MPa [ksi]**	**Strain at Ultimate Tensile Strength, Percent**
Titanium Aero Plate 6AL-4V Grade 5 per ASTM B265	943 [136.8]*	1,153 [167.4]	14.8
Hastelloy C22 Plate per ASTM B575	338.0 [49.1]*	1,213 [176.0]	49.0

*Yield stresses based on the secant at 0.2 percent

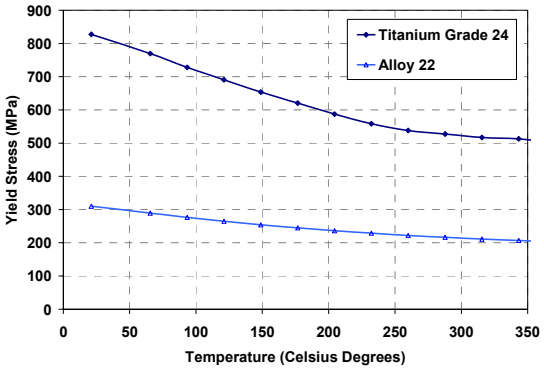

(a)

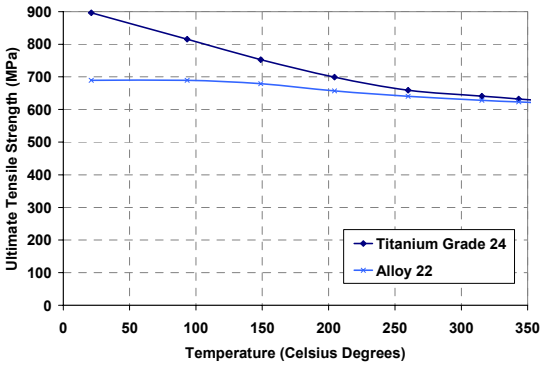

(b)

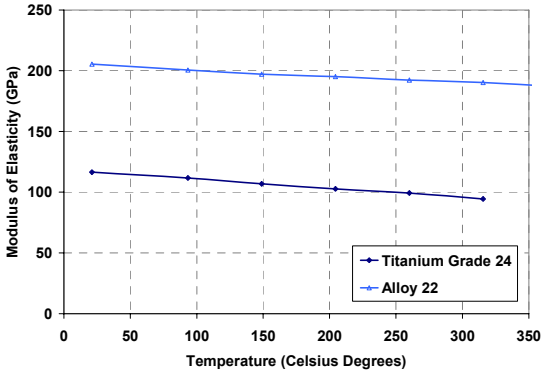

(c)

Figure 2-7. Effect of Temperature on Material Properties. (a) Yield Stress, (b) Ultimate Tensile Strength, (c) Modulus of Elasticity (ASME International, 2004). [1 MPa = 0.145 ksi, 1 GPa = 145 ksi, Fahrenheit Degrees = 1.8 × Celsius Degrees + 32]

3 EXPERIMENTAL RESULTS

This chapter presents the response obtained for the proof of concept experiment testing, DS– 45–01. This first test is used to demonstrate that the implemented process is sufficiently controlled and to provide preliminary experimental results that can be compared to the numerical models developed by Ibarra, et al. (2007b). The test nomenclature stands for drip shield–waste package experiment (DS), 45° titanium penetrator (45), and first testing for this configuration (01).

3.1 Proof of Concept Experiment (DS–45–01)

The test DS–45–01 consists of a titanium "drip shield" plate contacting an Alloy 22 "waste package" plate at an angle of 45°. The test was performed at room temperature using the test configuration described in Chapter 2 and presented in Figure 3-1. Note that the bottom of the Alloy 22 plate rests directly on the lower platen of the load frame and is partially constrained from motion by the waste package holder.

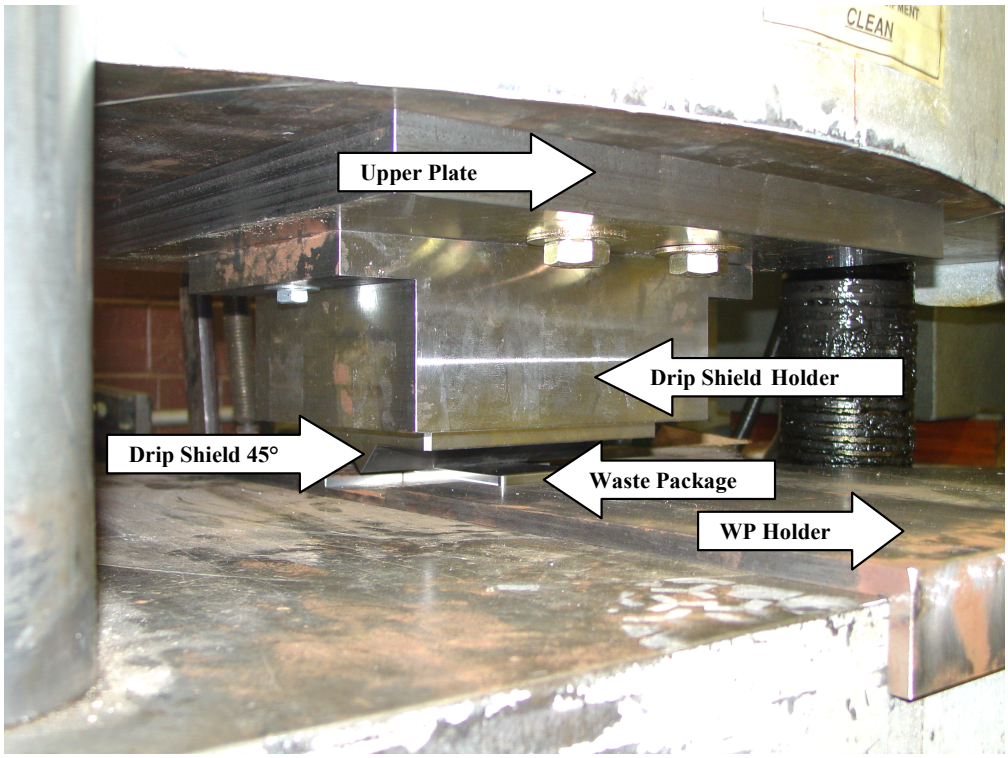

Figure 3-1. Load Frame Configuration for DS–45–01 Test

3.1.1 Loading

This test was performed at room temperature {24.4 °C [76 °F]} under a displacement rate of 25.4 mm/min [0.01 in/min]. The threshold parameters for load application were the machine load capacity {1,779 kN [400 kips]} and a deformation of 8.26 mm [0.325 in] for both the titanium and Alloy 22 plates. The specimen was initially loaded to 4.49 kN [1.01 kips] and, to establish a common starting point, this load was held for a short period of time. The displacement between plates was 0.0259 mm [0.001 in] for this initial load. The loading was then monotonically increased and discontinued after the maximum displacement of 8.265 mm [0.3254 in] was reached. The recorded load at this displacement was 1,690 kN [379.9 kips] (Figure 3-2). In this test, the Alloy 22 plate was wedged into the waste package holder due to large plastic deformations developing at the V-shaped groove. As observed in Figure 3-3, the Alloy 22 plate bulged outward at each free end of the V-shaped groove. There was also contact between the ends of the plate and the waste package holder. As shown in the following sections, the permanent deformation of the titanium plate was significantly smaller than that of the Alloy 22 plate.

3.1.2 Load-Displacement History

The applied load-displacement history between the upper and lower platens of the load frame is presented in Figure 3-4. The relationship is initially linear, and after softening in a short interval, the response becomes stiffer and quasi-linear again. The curve may be stiffer in the second half of the experiment because the large Alloy 22 plate deformation increased the contact of this plate with the waste package holder. Because the length of the Alloy 22 plate is 76.2 mm [3.00 in], the distributed load on the plate is 22,178 kN/m [1,520 kips/ft]. The following equation can be used to convert the force-per-unit length to the equivalent vertical pressure on the waste package.

$$P_{v,WPcap} = \frac{F_{unit}}{A_{trib}} L_{cont} \tag{3-1}$$

where F_{unit} is the force per unit length and A_{trib} is the tributary area of the drip shield bulkhead or stiffener (i.e., the area of drip shield crown that transfers loads throughout the evaluated drip shield component). Although A_{trib} is a variable parameter, its value is set at 2.3 m^2 [24.8 ft^2] for this study (Ibarra, et al., 2007b). The term L_{cont} is the contact length, which is independent of the tributary area in Eq. (3-1) because all the loads at the drip shield crown are assumed to be transferred to the waste package. Then, for F_{unit} = 22,178 kN/m [1,520 kips/ft] and assuming L_{cont} = 0.5 m [1.64 ft], the distributed load results in an equivalent vertical pressure of $P_{v,WPcap}$ = 4,820 kPa [699.6 psi]. This equivalent $P_{v,WPcap}$ is about 16 times larger than the expected vertical static pressure of about 300 kPa [43.5 psi] (Ibarra, et al., 2007a,b).

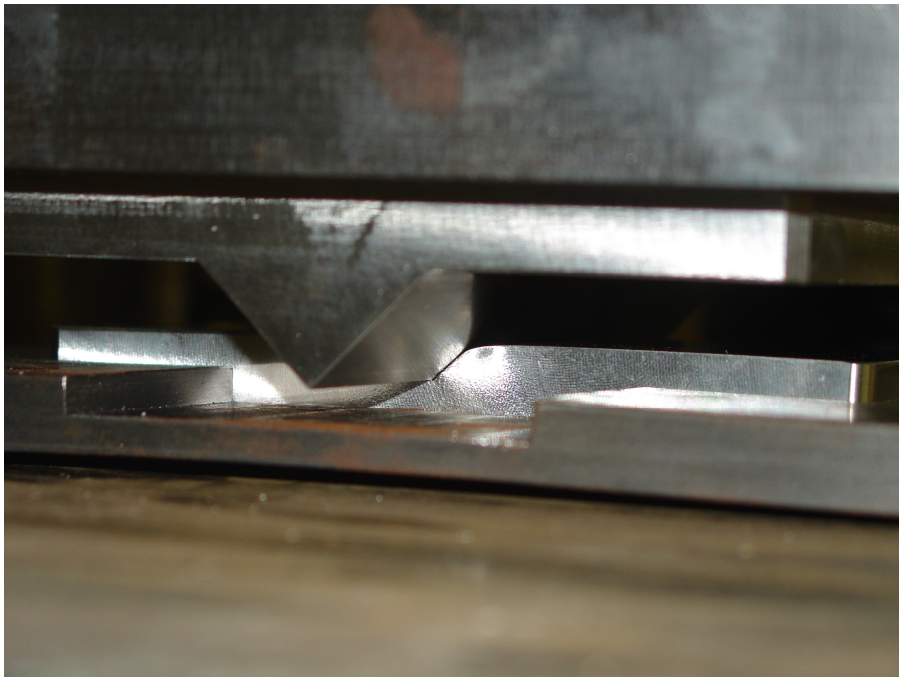

Figure 3-2. Test DS–45–01 at Maximum Applied Load

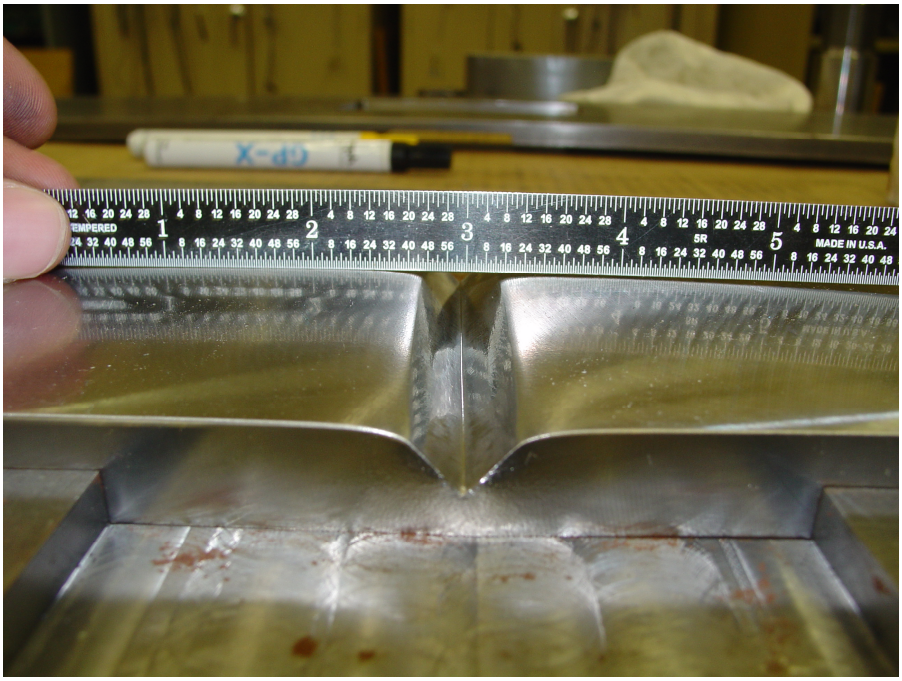

Figure 3-3. Permanent Deformation of Alloy 22 Plate in Test DS–45–01

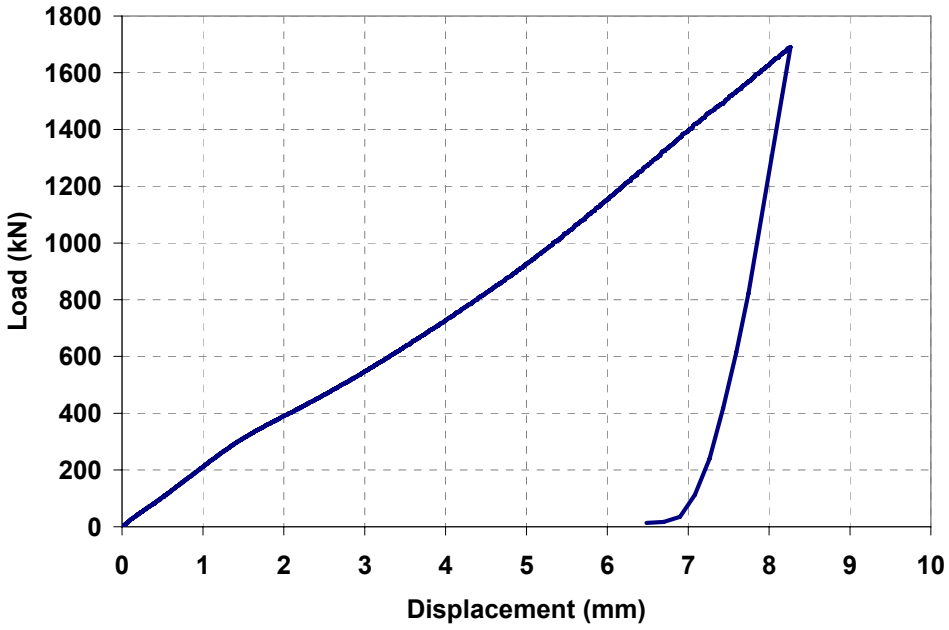

Figure 3-4. Load-Displacement Curve for Test DS–45–01; Units: kN and mm [1 kN = 0.225 kips, 1 mm = 0.039 in]

Note that the maximum displacement of 8.265 mm [0.3254 in] is caused by the deformation of both plates. For an applied force equivalent to a expected vertical static pressure of 300 kPa [43.5 psi], the total deformation is 0.52 mm [0.0205 in]. Figure 3-4 also shows that during unloading, the rate is initially linear and becomes highly nonlinear prior to loss of contact, resulting in a permanent displacement for both plates of 6.48 mm [0.255 in].

3.1.3 Measurement of Plates Permanent Deformation

For the DS–45–01 testing, the permanent plastic deformations of both plates were measured using the DSL and CMM methods.

3.1.3.1 Plates Permanent Deformations According to the DSL Method

The DSL method provides a complete scan of the surface of the test items. To smooth the surface profile, a thin coat of flat white paint was sprayed onto the surface, and the depth of the groove in the center of the Alloy 22 plate was measured as 5.72 mm [0.225 in] (Figure 3-5). For the titanium penetrator, the height of the apex at its center was measured as 18.39 mm [0.724 in] (Figure 3-6). Because the initial height of the titanium penetrator was 19.05 mm [0.75 in], the depth of the groove was reduced 0.66 mm [0.026 in]. Then, the plastic deformation for both plates is 6.38 mm [0.252 in]. This value is close to the 6.48 mm [0.255 in] measured after the specimens are unloaded (Figure 3-4).

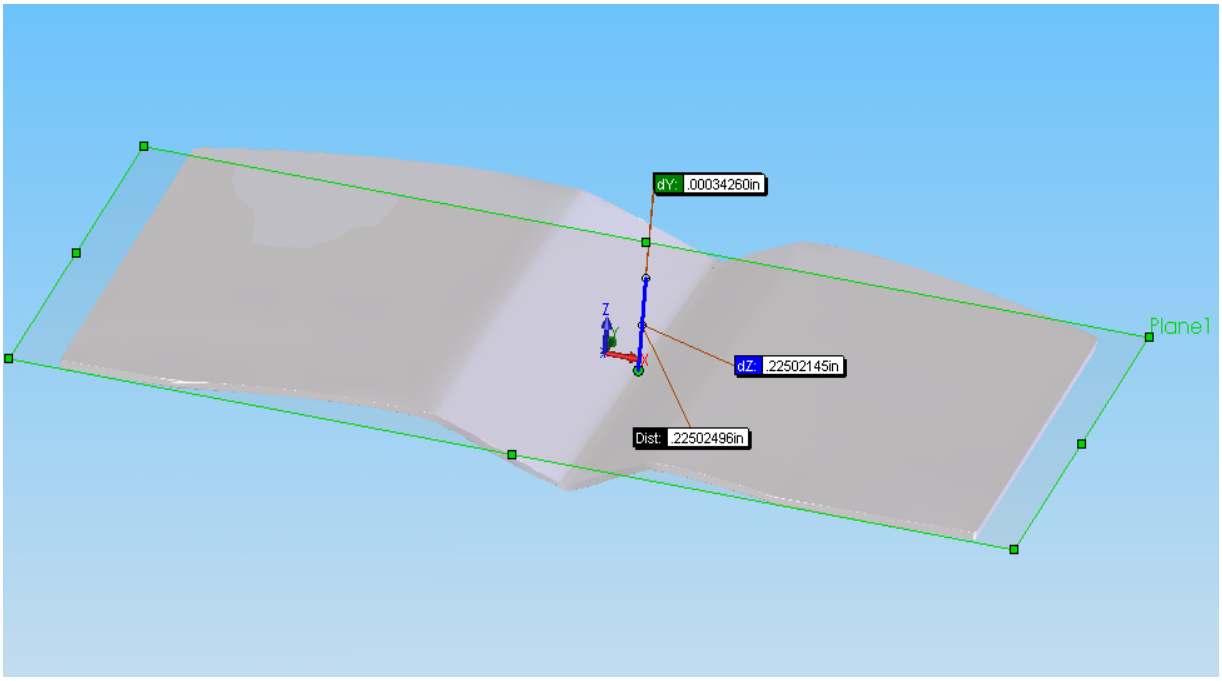

Figure 3-5. DSL Scan of DS–45–01 Alloy 22 Plate [1 in = 25.4 mm]

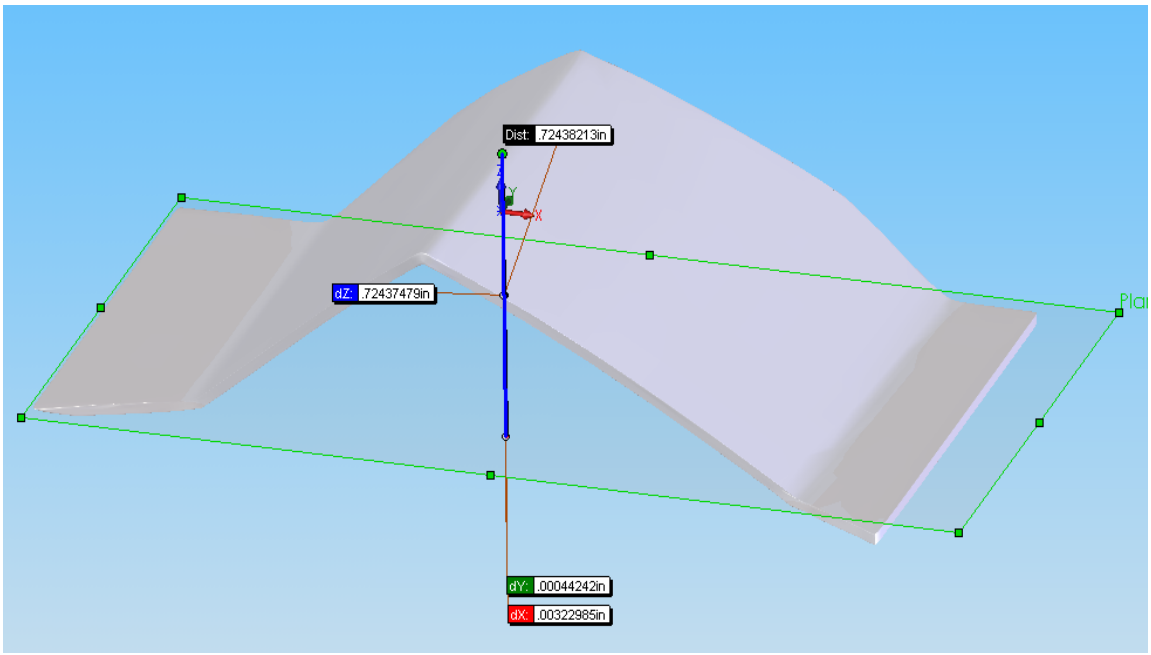

Figure 3-6. DSL Scan of DS–45–01 Titanium Penetrator [1 in = 25.4 mm]

The groove depth of the deformed Alloy 22 plate subjected to the applied load can be obtained by assuming that the plastic deformation of the titanium penetrator is approximately the total deformation of this component. Therefore, the titanium penetrator deformation, 0.66 mm [0.026 in], is subtracted from the total deformation of both plates measured during loading, 8.265 mm [0.325 in], resulting in an Alloy 22 groove depth of 7.61 mm [0.30 in].

3.1.3.2 Permanent Plate Deformations According to the CMM Method

In this method, a line scan was run perpendicular to the line of the load. The Y (width) and Z (vertical) coordinates of these points were measured for each of the X (length) points. For the Alloy 22 plate, geometric transformations were used to identify the deformation of the groove depth because the top surface of the plate also exhibited permanent deformation (Figure 3-7). The estimated range for the groove depth was from 6.10 to 6.18 mm [0.240 to 0.255 in] (Figure 3-8), which are larger values than those obtained from the DSL method {5.72 mm [0.225 in]}. Note that the average angle of the groove slope is approximately 50° after stress relaxation.

For the titanium plate, a line scan was also run perpendicular to the line of the load. Because the plate does not remain flat, geometric transformations were applied. The first transformation mapped the data points of the titanium penetrator to a flat surface centered about the line of the load (Figure 3-9). The measured reduction of the height of the apex of the titanium plate was 0.72 mm [0.0285 in], which is also larger than the measurement obtained using the DSL method {0.66 mm [0.026 in]}.

The second transformation assumed that the lower portions of the sloped sides of the groove did not deform. The initial data from the CMM scan was first rotated such that the slopes in the undeformed regions were equal. Lines were extrapolated from the underformed slopes and the intersection was assumed to be at the initial tip of the groove {i.e., at 19.05 mm [0.75 in]}. The deformed peak for DS–45–01 was located at 17.79 mm [0.7005 in], and the reduction of the height of the apex was 1.25 mm [0.0495 in]. This deformation is greater than that obtained from the DSL method and the CMM method using the first transformation. The assumption of “undeformed” segments may not be appropriate, because the calculated angle of each side is 45.9°, instead of the original 45°.

The total deformation for both plates, assuming the first transformation for the titanium plate data, ranges from 6.82 mm [0.2685 in] to 6.90 mm [0.2835 in]; the groove depth of the deformed Alloy 22 plate when subjected to the applied load is 7.53 mm [0.2965 in]. Both measurement methods render similar results that are in accordance with the load-displacement curve obtained directly during the test.

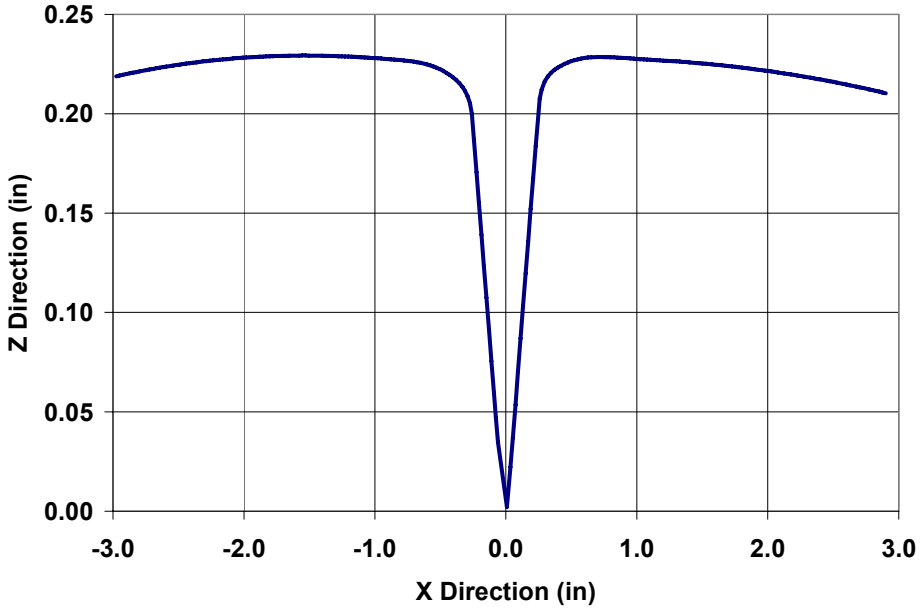

Figure 3-7. CMM Scan in X Direction for DS–45–01 Alloy 22 Plate [1 in = 25.4 mm]

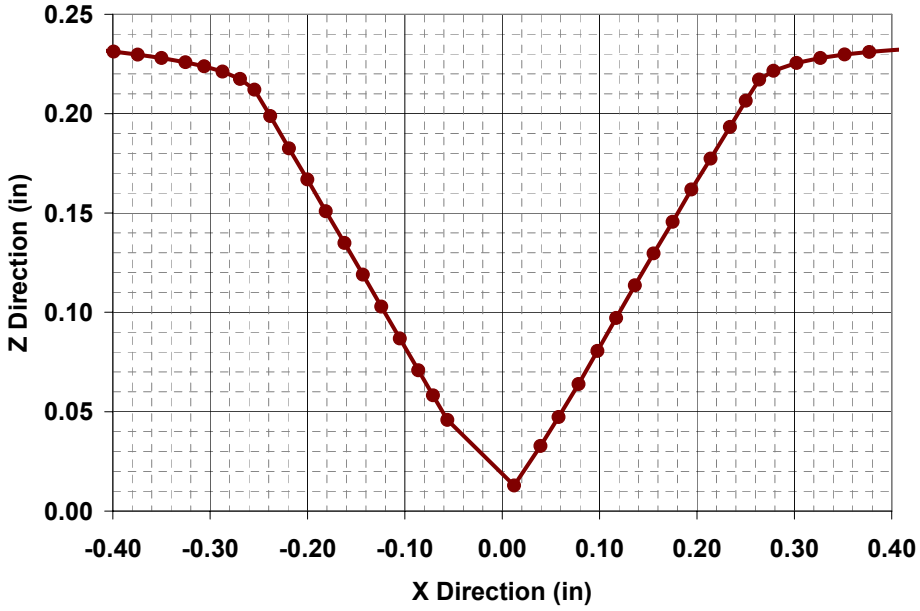

Figure 3-8. Detail of CMM Scan in X Direction for DS–45–01 Alloy 22 Plate [1 in = 25.4 mm]

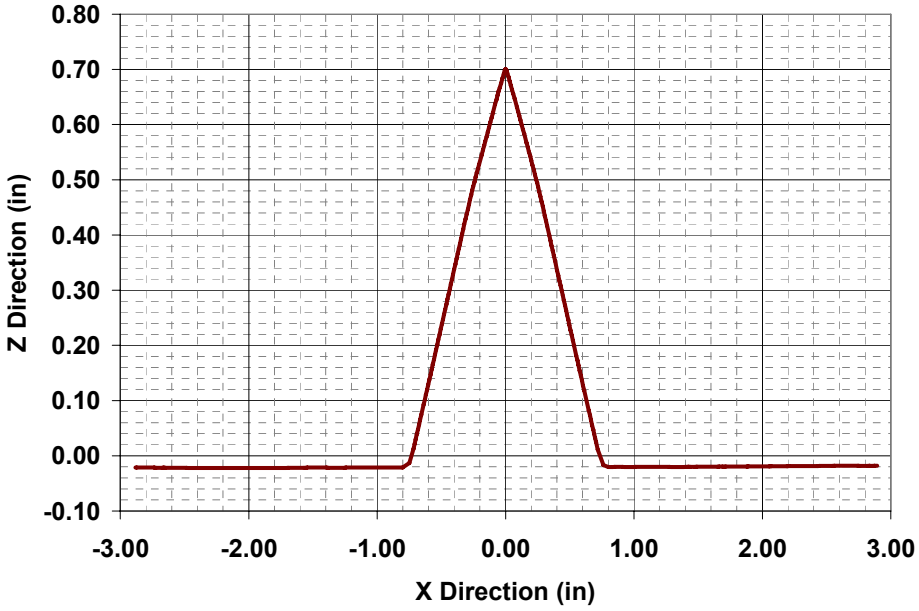

Figure 3-9. CMM Scan in X Direction of DS–45–01 Titanium Penetrator [1 in = 25.4 mm]

4 COMPARISON OF EXPERIMENTAL AND NUMERICAL PLANE STRAIN MODELS

4.1 Description of Two-Dimensional Plane Strain Model

Ibarra, et al. (2007b) developed plane strain finite element models to evaluate the potential for waste package failure due to mechanical interaction with a collapsed drip shield. The models were created in ABAQUS (ABAQUS, Inc., 2004) using simple geometric representations of the engineered barrier components that permitted the use of highly refined meshes (Figure 4-1). The models are based on the assumption that the displacement in the longitudinal direction (out-of-plane) of the stiffener or bulkhead is orders of magnitude smaller than the displacements in the transverse direction (in-plane). In the model, the edges of the drip shield components are rounded by introducing a radius of 0.25 mm [0.01 in] at the edge of the drip shield component. This ensures an initial small contact width between the drip shield and waste package components when the first contact occurs. Note that the same radius for the titanium penetrator was used in the experimental test.

The drip shield component is loaded by a distributed body force, and the resultant of this body force equals the total applied load that the stiffener or bulkhead would carry from the corresponding tributary area of the drip shield. The plate simulating the waste package outer shell is constrained on one side from moving in the horizontal direction (1-axis), but is free to move on the opposite side to allow horizontal expansion. Also, the waste package outer shell bottom surface is constrained from moving in the vertical direction (2-axis). This last constraint simulates the assumed rigid surface for the inner vessel. The bulkhead and stiffener components have roller supports that only allow vertical translation. Two vertical springs with a very small stiffness are used to prevent initial rigid body translation in the vertical direction.

The plane strain model was evaluated for different contact angles and drip shield components. The model with the bulkhead and longitudinal stiffeners is represented in Figure 4-1 (Ibarra, et al., 2007b). Because the geometry of the waste package and drip shield design prevents large contact angles, it was considered that contact angles under most of the loading scenarios would be less than 15°, although the 45° case of the experimental study was also evaluated. The study concluded that in addition to the static and dynamic loading, the waste package vertical load carrying capacity is largely affected by the contact angle and the contact length. Both parameters are directly related to the contact area between the drip shield and waste package components. However, only the effect of the contact angle can be evaluated in this experimental study.

4.2 Numerical Failure Mode for Plane Strain Models

Waste package failure refers to breaching of the Alloy 22 waste package outer shell and is physically associated with cracks that propagate through its thickness. The numerical waste package outer shell failure mode, however, is associated with the first elements reaching the ultimate tensile strength. Thus, this failure limit state only predicts the onset of waste package breaching, but it has the advantage of only requiring finite element models with nondeteriorating constitutive relationships (e.g., the models do not include strength and stiffness deterioration). The failure limit state is expressed in terms of the waste package vertical load carrying capacity (i.e., the vertical load the waste package can withstand without reaching the ultimate tensile strength of the Alloy 22 material).

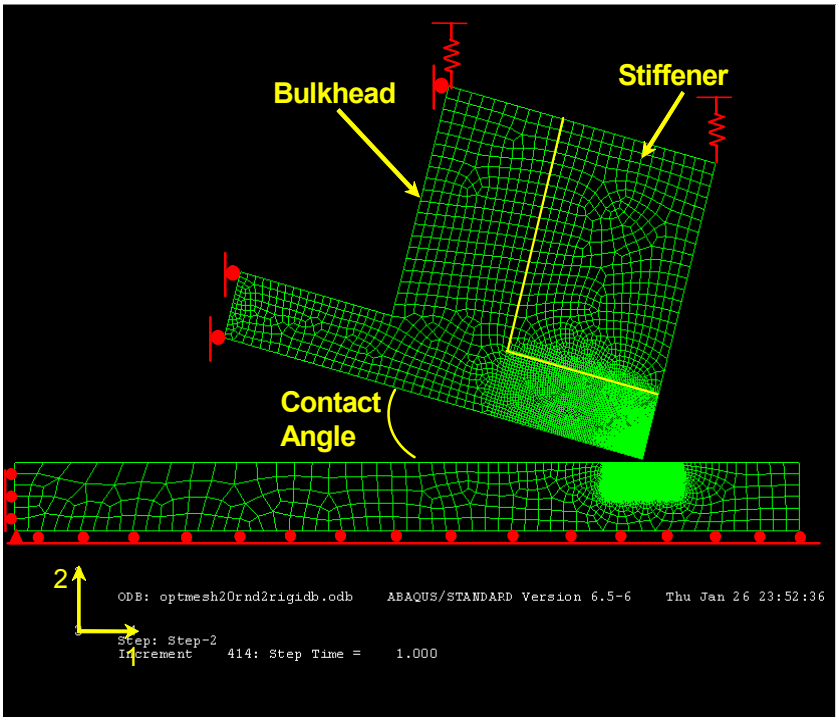

Figure 4-1. Two-Dimensional Plane Strain Finite Element Model; Bulkhead Cross Section With Longitudinal Stiffener and Waste Package Outer Shell

The numerical failure mode definition assumes that stress corrosion cracking is highly unlikely in Alloy 22 in the Yucca Mountain environmental conditions and that localized corrosion does not affect mechanical stresses. On the other hand, the following factors may induce different degrees of conservatism in the response of these models:

- The assumption of failure occurring as soon as the first Alloy 22 element reaches the ultimate tensile strength induces a conservatism that is difficult to estimate. As the drip shield component penetrates into the Alloy 22 plate, waste package breaching may be arrested because of the increase in the contact area, even if some elements reach the ultimate tensile strength. Alternatively, failure of the first finite elements may propagate and lead to a band of damaged elements with no strength resistance, which may not be arrested even if the contact area increases.

- Failure strains are defined as the strain at ultimate tensile strength. After the ultimate tensile strength is surpassed, the Alloy 22 engineering stress-strain curve exhibits a steep negative slope that ends when failure strain is reached. A system with no redundancy subjected to monotonic loads would become structurally unstable if the ultimate strength is surpassed. In the case of the waste package outer shell, however, the redundancy provided by the system geometric characteristics would allow stress redistribution.

- The drip shield components may reach the ultimate tensile strength prior to numerical failure of the Alloy 22 material. Because nondeteriorating models do not lose resistance capacity, the drip shield component resistance may be overestimated, leading to smaller contact areas than those expected in the physical models.

4.3 Comparison of Experimental and Numerical Model Results

The numerical plane strain models (Ibarra, et al., 2007b) predict that for a contact angle of 45° and mechanical properties at 150 °C [302 °F], a load of 10,780 kN/m [738 kips/ft] has to be applied to the waste package to reach the numerical limit state of some Alloy 22 elements. The model, however, was reevaluated for this study to use the as-received material properties of the components at room temperature (Table 2-3). Figure 4-2 presents the plastic strains for the numerical waste package failure limit state. As observed, the new analysis indicates that the waste package vertical load carrying capacity is reduced to 5,108 kN/m [350 kips/ft] and the groove depth is only 1 mm [0.004 in]. The waste package capacity reduction is caused by modifications to the material properties of both plates. As observed in Tables 2-2 and 2-3 and Figure 2-7, the Alloy 22 material properties are not significantly modified, though the strain at ultimate failure is reduced from 0.55 to 0.49. More significant is the increase of the as-received titanium material properties at room temperature with respect to the properties obtained from the standard at 150 °C [302 °F]. The stronger titanium material would penetrate more rapidly into the Alloy 22 material.

Based on the failure limit state definition provided in Ibarra, et al. (2007b), the applied load would be interrupted at the level presented in Figure 4-2 because the nondegrading finite element model may overestimate the overall waste package performance due to elements exceeding the ultimate tensile strength measured in terms of the effective plastic strain (PEMAG). To evaluate the extent of this potential overestimation, the load was increased to the total load applied to the experimental test DS–45–01. Figure 4-3 shows the experimental load-total displacement history (e.g., the displacement between the Alloy 22 and titanium plate surfaces), as well as the load versus Alloy 22, titanium, and total numerical displacement histories. As can be seen, the numerical and experimental load-total deformation relationships are in good agreement not only prior to the reaching of the numerical limit state, but also after this threshold is surpassed, in spite of using a numerical model that cannot account for the strength and stiffness degradation of the elements reaching the ultimate tensile strength. The load-displacement curves also show a change of slope at the level where the numerical model predicts that some Alloy 22 elements exceed the ultimate tensile strength.

The good correlation between the titanium and Alloy 22 load-displacement curves after the numerical failure limit state is exceeded indicates that the local failure of the Alloy 22 elements contacting the tip of the titanium penetrator does not propagate rapidly. In addition, failure appears to be self-arrested by the increase of the contact area, as the titanium material penetrates the Alloy 22 plate. This can be observed in the Von Mises stress and plastic strain distributions at the maximum experimental load presented in Figures 4-4 and 4-5, respectively. In these figures, the elements exceeding the ultimate tensile strength are confined to the green zone surrounding the tip of the groove. Note the elements largely exceeding the ultimate tensile strength are highly concentrated at the tip of the groove. The performance of the Alloy 22 plate after the first elements reach the ultimate tensile strength leads to experimental loads that are about two times the loads initially predicted by Ibarra, et al. (2007b) for the numerical failure limit state.

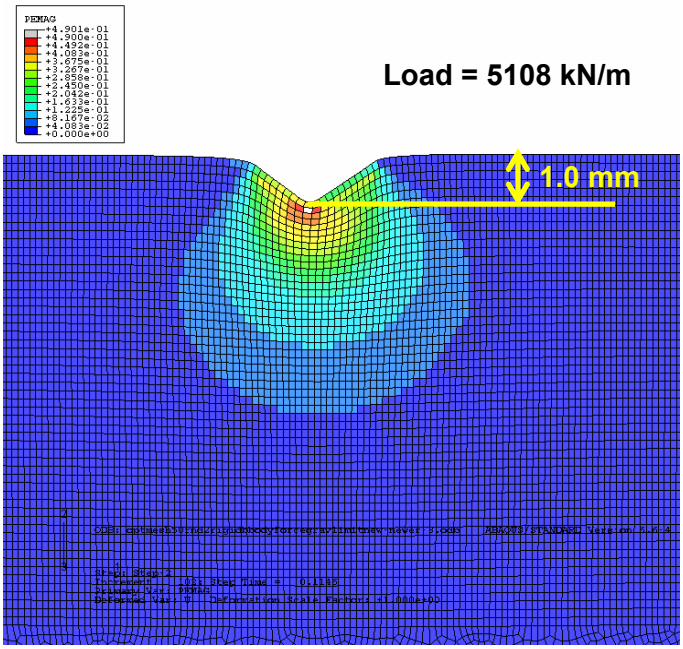

Figure 4-2. Plastic Strain Distribution of Alloy 22 Plate at the Ultimate Tensile Strength [1 kN/m = 0.069 kips/ft]

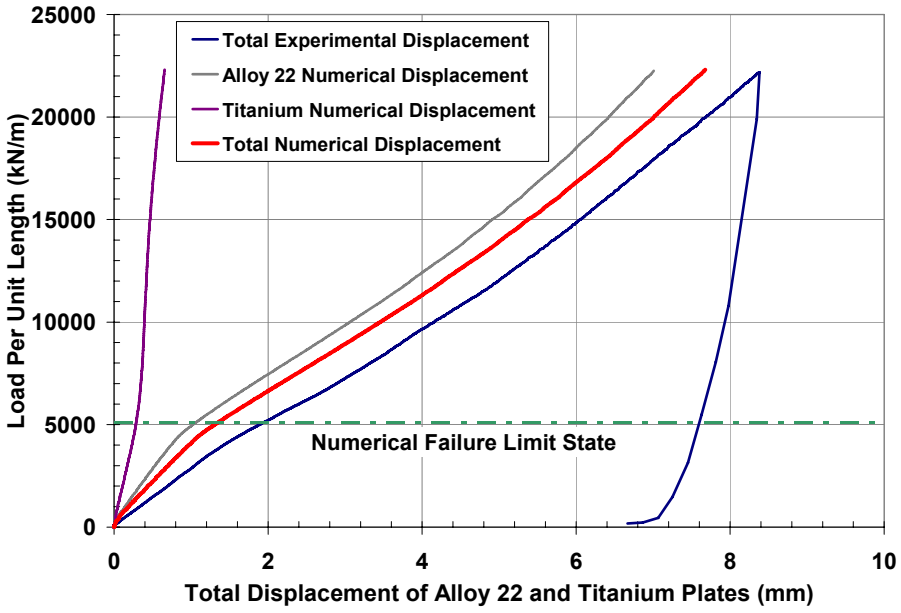

Figure 4-3. Experimental (DS–45–01) and Numerical Load-Displacement Relationships [1 kN/m = 0.069 kips/ft, 1 mm = 0.039 in]

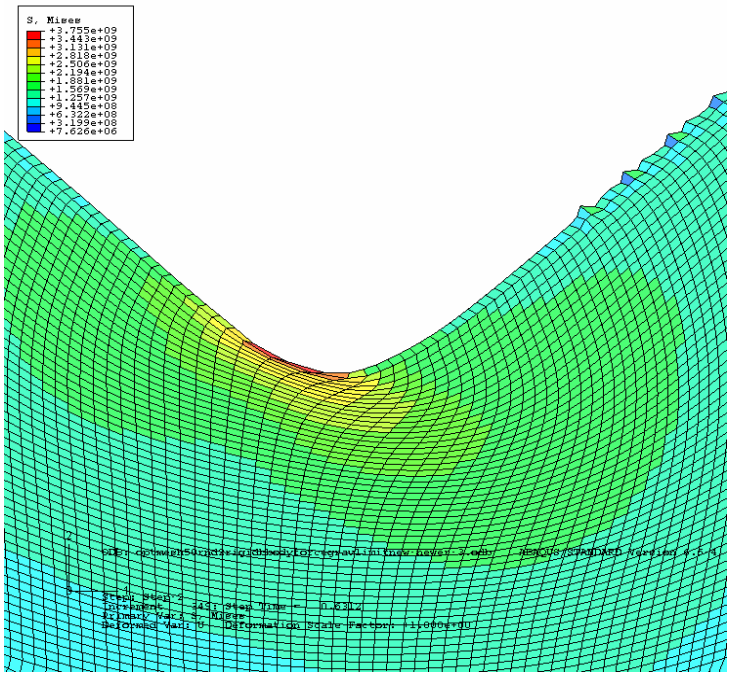

Figure 4-4. Von Mises Stress Distribution of Alloy 22 Plate at the Maximum Experimental Load of DS–45–01 {Units: Pa [1 Pa = 0.145 × 10^{-3} psi]}

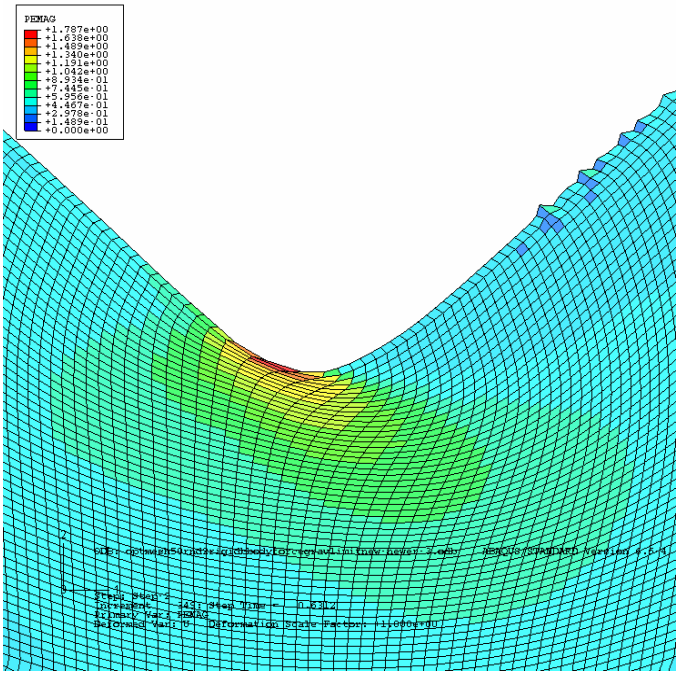

Figure 4-5. Plastic Strain Distribution of Alloy 22 Plate at the Maximum Experimental Load of DS–45–01

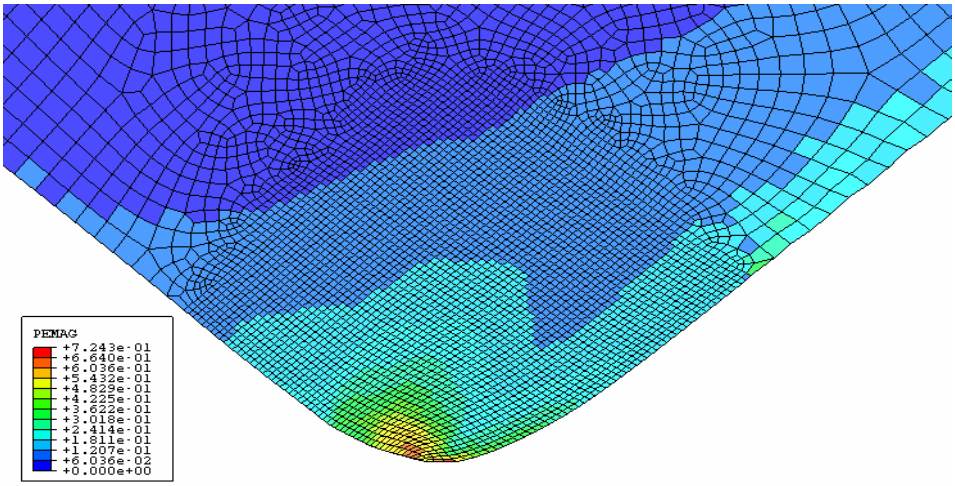

Figure 4-6. Plastic Strain Distribution of Titanium Plate at the Maximum Experimental Load of DS–45–01

Furthermore, the experimental loads obtained from test DS–45–01 are more than four times the loads predicted by the numerical models that implement the as-received material mechanical properties at room temperature.

The load-displacement curves for the titanium material result in a displacement of 0.66 mm [0.025 in] at the penetrator apex, which is very close to the plastic deformation obtained from the DSL and CMM methods (Chapter 3). This titanium deformation was estimated as the displacement differential between the tip and the top point of the highly refined mesh region (Figure 4-6). This point was considered appropriate because it comprises the region experiencing plastic strains at the tip of the penetrator.

5 SUMMARY AND CONCLUSIONS

The drip shield and waste package are part of several engineered barrier subsystems that DOE is considering for the potential geologic repository at Yucca Mountain, Nevada, where the radioactive waste materials would be encapsulated in waste packages and emplaced in tunnels. The drip shield protects the waste package from rockfall impacts and water intrusion. Independent structural analyses (Ibarra, et al., 2007a), however, indicate that the drip shield design DOE is currently considering (Bechtel SAIC Company, LLC, 2004a) may not be able to withstand the expected static and dynamic loading conditions that might result from rockfall rubble accumulation. The potential drip shield structural instability may result in drip shield–waste package mechanical interaction, which could lead to high localized plastic stresses in the waste package.

The waste package consists of an external cylinder (outer shell) made of Alloy 22 material and a stainless steel internal cylinder (inner vessel). Waste package failure is defined as breaching of the Alloy 22 waste package outer shell by the propagation of cracks through its thickness (Ibarra et al., 2007b). Thus, the waste package inner vessel function is limited to providing structural support. Numerical plane strain finite element models have been used to evaluate the potential for waste package breaching due to mechanical interaction with a collapsed drip shield (Ibarra, et al., 2007b). The failure limit state for the models refers to the vertical load at which the waste package outer shell material reaches the ultimate tensile strength (peak strength).

To verify the structural performance obtained from the plane strain models, an experimental study was performed to evaluate the capacity of Alloy 22 plates when subjected to loads transferred by Titanium Grade 5 [surrogate for Titanium Grade 24 (Ankem and Wilt, 2006)] plates with different inclination angles (e.g., contact angle). This progress report describes the experimental setup used to reproduce the conditions of the numerical plane strain models, as well as the plate deformation measurement techniques. The experimental tests provide a response comparison for the loading range evaluated in the numerical models. More importantly, the tests provide the performance of the Alloy 22 material for nonlinear states that cannot be predicted by only using finite element models with nondegrading constitutive relationships.

The report presents the results of the first experiment in which the contact angle between the titanium and Alloy 22 plates is 45°. The test was performed at room temperature under a displacement rate of 25.4 mm/min [0.01 in/min]. The loading was monotonically increased and discontinued after the maximum displacement of 8.265 mm [0.3254 in] was reached. The recorded load at this displacement was 1,690 kN [379.9 kips], equivalent to a load per unit length of 22,178 kN/m [1,520 kips/ft]. This load is about two times the load initially predicted by Ibarra, et al. (2007b) for the numerical failure limit state, but more than four times the load predicted by the numerical models when using the as-received material properties at room temperature. The difference in the numerical model results appears to be caused by the relatively large increase in the titanium material properties as the temperature decreases. Also, the experimental load is approximately one order of magnitude larger than the expected vertical static pressure at the crown of the drip shield.

The experimental and numerical load-displacement relationships, however, showed good agreement until the maximum load applied to the experimental test. In fact, the

load-displacement curves correctly predicted the change of slope in the load-displacement curve at the loading level that causes some Alloy 22 elements to exceed the ultimate tensile strength. The good correlation between the titanium and Alloy 22 load-displacement curves after the numerical failure limit state is exceeded indicates that the local failure of the Alloy 22 elements contacting the tip of the titanium penetrator does not propagate rapidly. In addition, failure appears to be self-arrested by the increase of the contact area, as the titanium material penetrates the Alloy 22 plate.

Two techniques were evaluated to measure the permanent deformation field of the Alloy 22 and titanium plates. First, a three-dimensional surface measurement was performed using a dynamic structured light technique that characterizes the overall surface geometry. The second technique was the coordinate measuring machine method, in which a stylus is moved across the surface of the material resulting in a line scan along the centerline of the plate. The results from both techniques were in good agreement with the deformation results obtained during the test.

The preliminary experimental results indicate that the numerical models used in the earlier stage of this study can reproduce the mechanical response of the drip shield–waste package mechanical interaction beyond the current failure limit state. The better than expected response of the Alloy 22 material led to very large plate deformations without evidence of through cracks from the bottom of the groove to the back side of the plate. Note that this performance only refers to the mechanical failure mode of Alloy 22 under static loading. The Yucca Mountain environment conditions could lead to cracks at lower vertical loads.

6 FUTURE WORK

The results presented in this progress report should be considered preliminary because they consider the response of only one experimental test. Several parameters that could affect this structural response may be evaluated in a potential second stage of this study:

- Contact angle—In addition to testing titanium plates with 45°angles, experiments would be performed using titanium penetrators with angles of 15° and 5°. The contact angle of 45° was used in this first stage because it represents a symmetric condition that does not generate horizontal reactions. Nevertheless, the contact angle between drip shield and waste package components is expected to be smaller than about 10-15° (Ibarra, et al., 2007b).

- Yucca Mountain Environmental Conditions—Some tests may be performed at temperatures and chemical environments that better reflect anticipated in-drift conditions.

- Boundary conditions—To determine the effect of boundary conditions on the Alloy 22 material, additional tests using 45° angle titanium penetrators may be performed. These tests would determine the influence of end constraints on the Alloy 22 waste package plate.

Initially, impact loading was expected to be evaluated to simulate the dynamic loading that may occur during a seismic event. This part of the project may not be performed because of the better than expected performance of the Alloy 22 plate when subjected to static loading.

7 REFERENCES

ABAQUS, Inc. "ABAQUS User's Manual." Version 6.5. Providence, Rhode Island: ABAQUS, Inc. 2004.

Ankem, S. and T. Wilt. "A Literature Review of Low Temperature (<0.25T_m) Creep Behavior of α, α-β and β Titanium Alloys." San Antonio, Texas: Center for Nuclear Waste Regulatory Analyses. 2006.

ASME International. "ASME International Boiler and Pressure Vessel Code." New York City, New York: ASME International. 2004.

Bechtel SAIC Company, LLC. "Drip Shield Structural Response to Rockfall." 000–00C–SSE0–00300–000–00A. Las Vegas, Nevada: Bechtel SAIC Company, LLC. 2004a.

———. "Mechanical Assessment of the Waste Package Subject to Vibratory Ground Motions." CAL–WIS– AC-000001. Rev. 00B. Las Vegas, Nevada: Bechtel SAIC Company, LLC. 2004b.

Brown, N.R. "Waste Package and Drip Shield Design." Presentation at the DOE/NRC Technical Exchange on Level of Detail, February 2004. Las Vegas, Nevada: U.S. Department of Energy, Office of Civilian Radioactive Waste Management. 2004.

Franke, E., M. Magee, J. Mitchell, and M. Rigney. "3D Precision Surface Measurement by Dynamic Structured Light." Proceedings Volume for Two- and Three-Dimensional Vision Systems for Inspection, Control, and Metrology. Vol. 5,265, No. 26. Bellingham, Washington: Society of Photographic Instrumentation Engineers. February 2004.

Ibarra, L., T. Wilt, G. Ofoegbu, and A. Chowdhury. "Structural Performance of Drip Shield Subjected to Static and Dynamic Loading." San Antonio, Texas: Center for Nuclear Waste Regulatory Analyses. 2007a.

Ibarra, L., T. Wilt, G. Ofoegbu, R. Kazban, F. Ferrante, and A. Chowdhury. "Drip Shield–Waste Package Mechanical Interaction." San Antonio, Texas: Center for Nuclear Waste Regulatory Analyses. 2007b.

APPENDIX

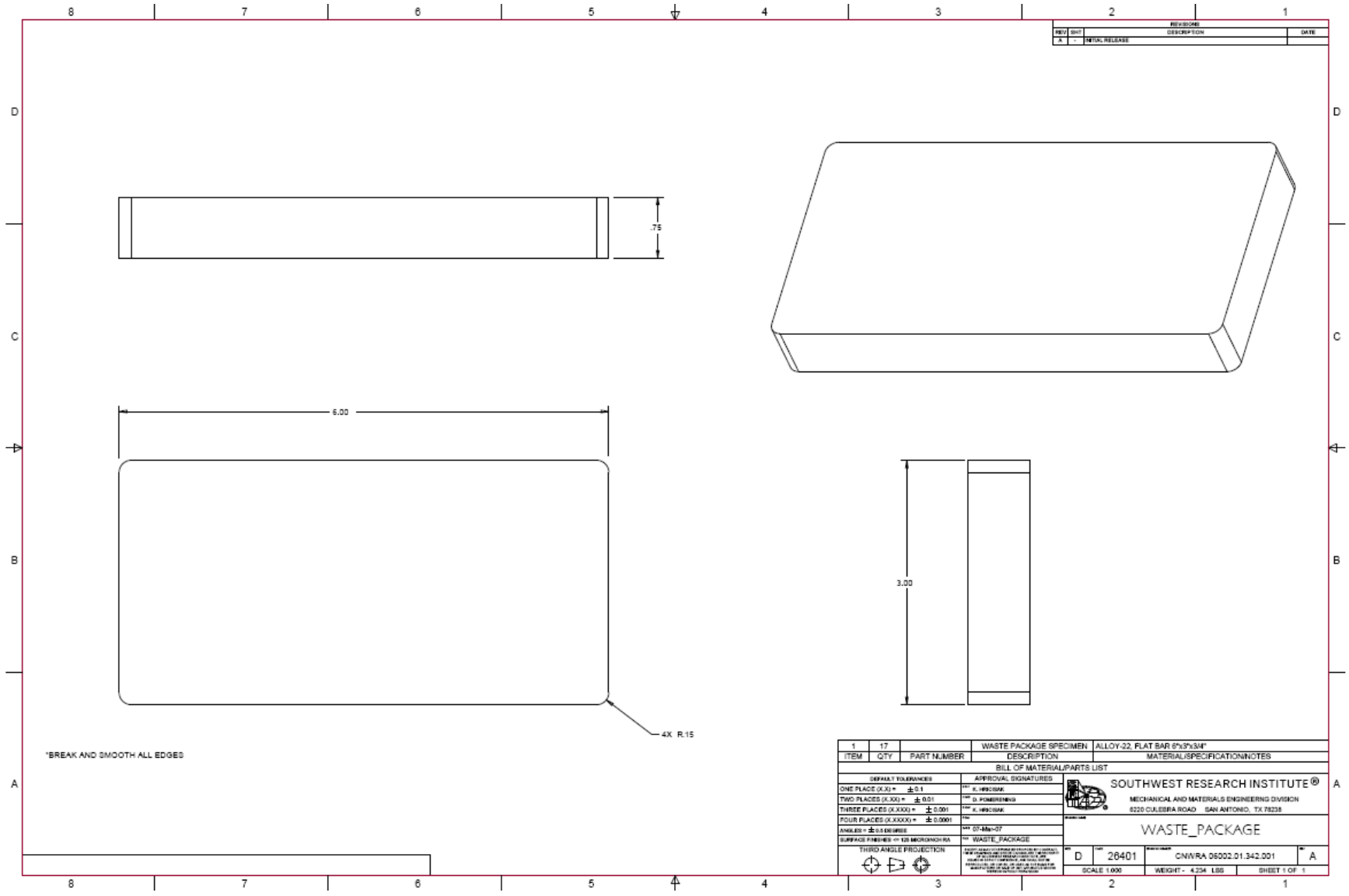

Figure 1. Alloy 22 "Waste Package Outer Shell." Dimensions in Inches [1 in = 25.4 mm].

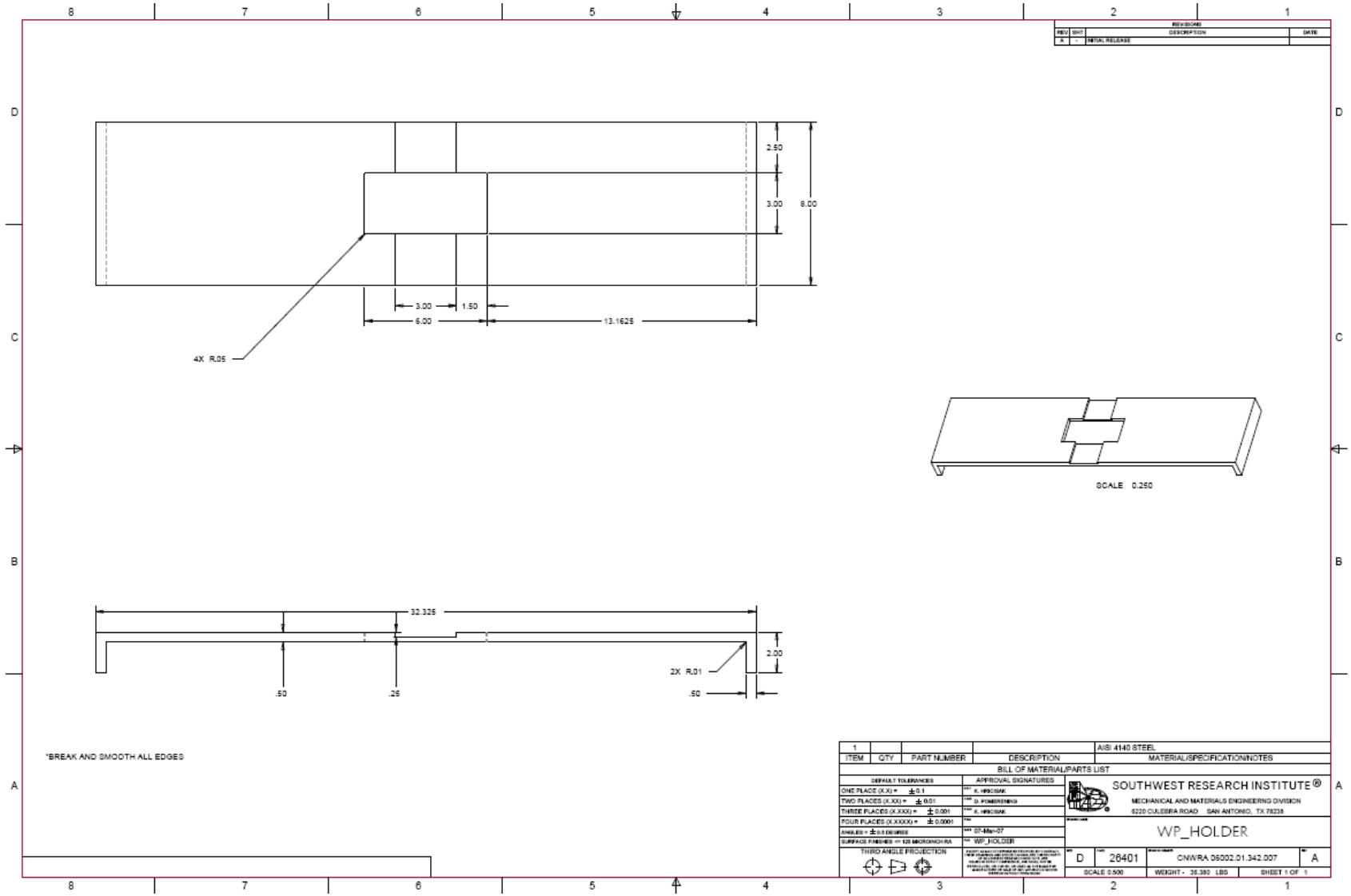

Figure 2. Steel Waste Package Holder. Dimensions in Inches [1 in = 25.4 mm].

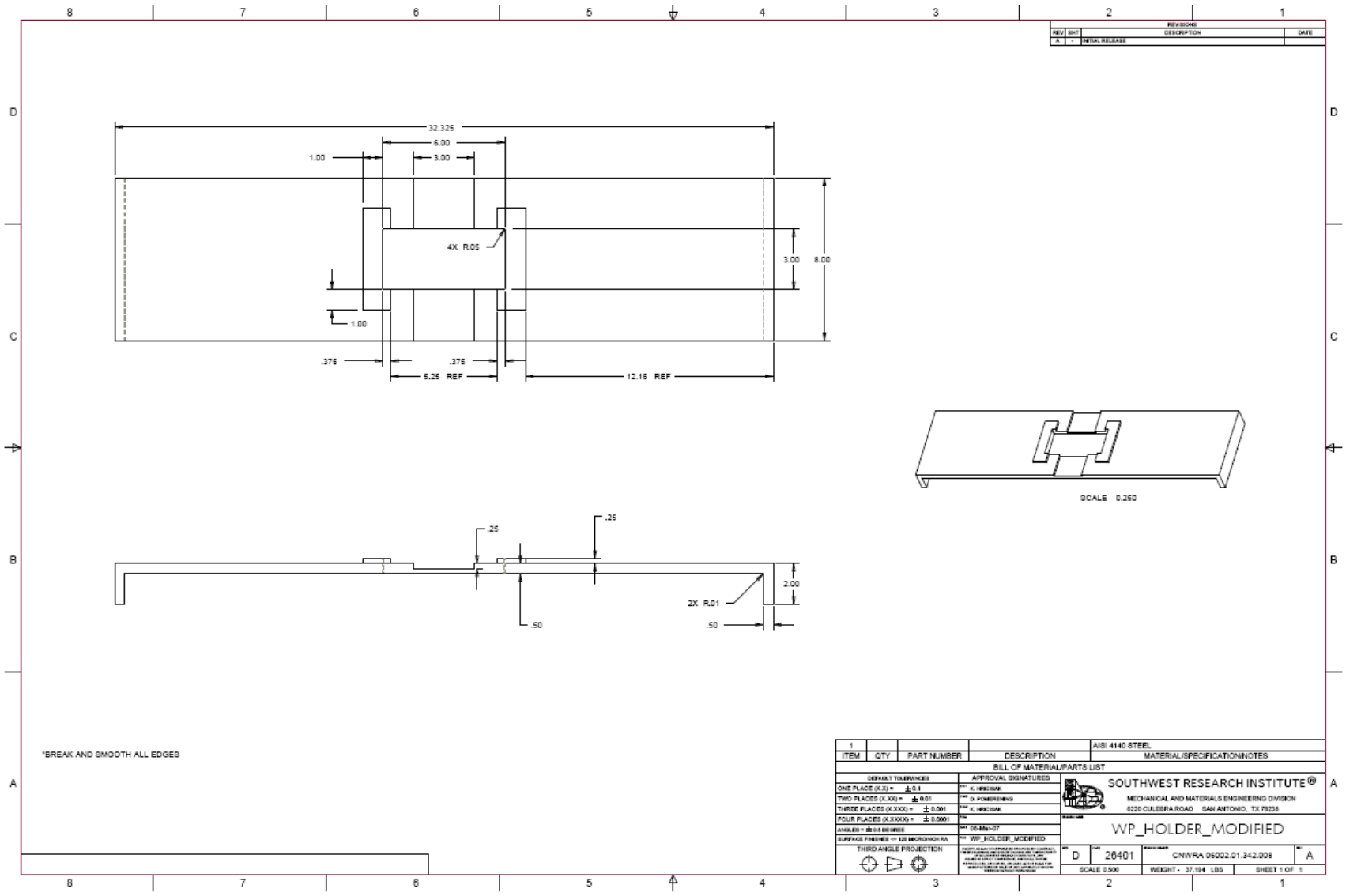

Figure 3. Modified Steel Waste Package Holder. Dimensions in Inches [1 in = 25.4 mm].

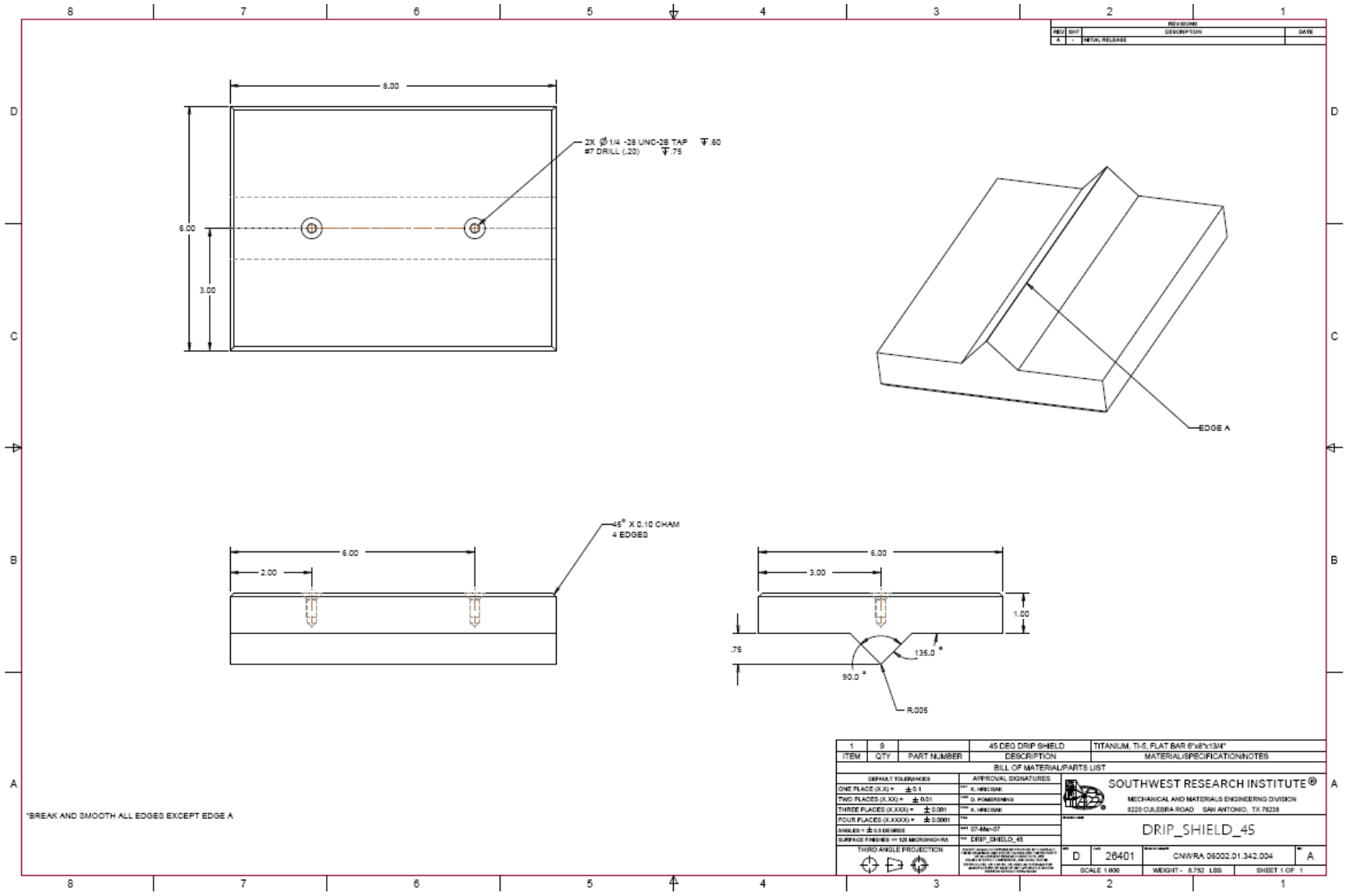

Figure 4. Titanium Grade 5 Plate Representing a Drip Shield Component With a Contact Angle of 45°. Dimensions [1 in = 25.4 mm].

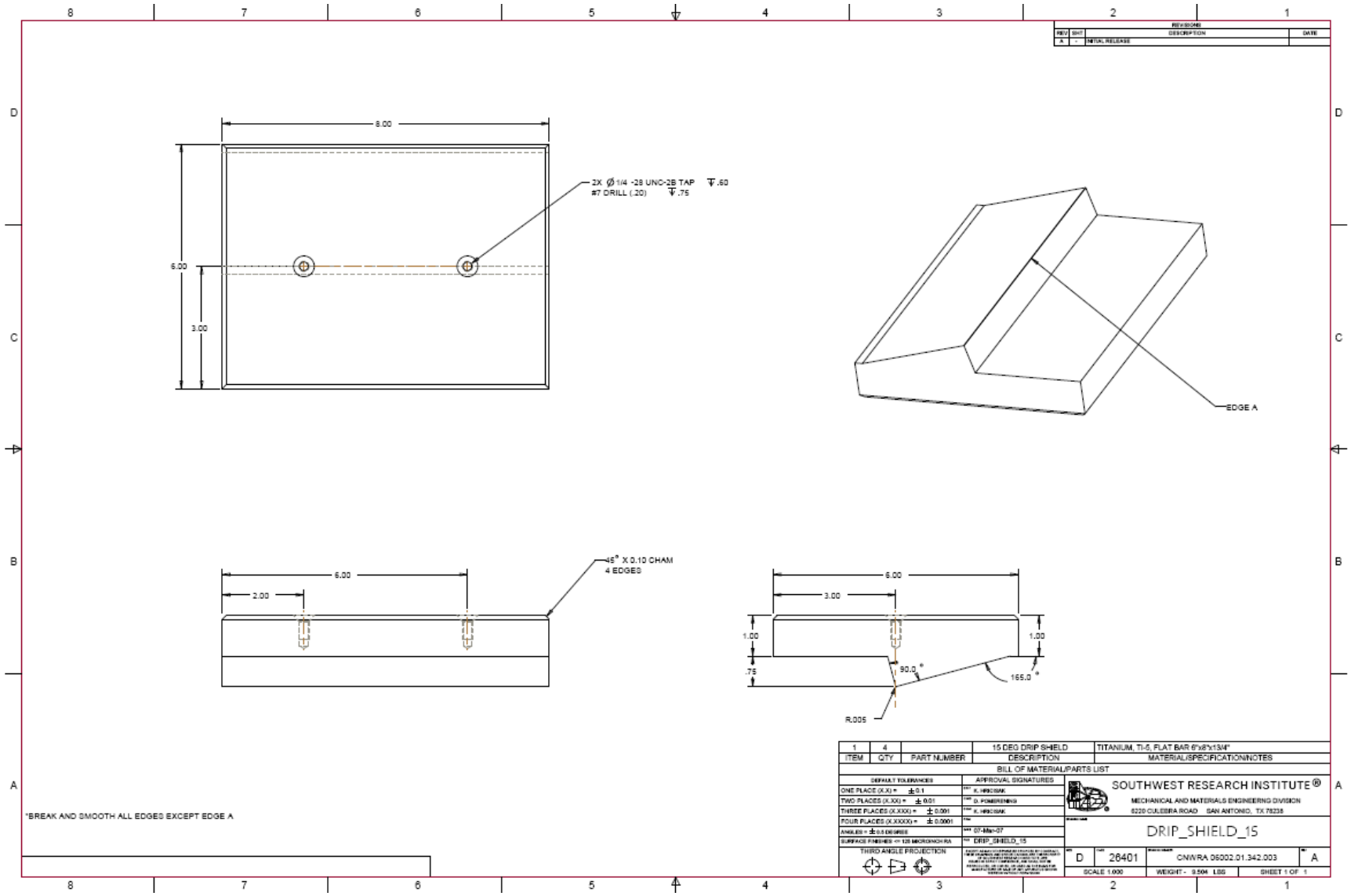

Figure 5. Titanium Grade 5 Plate Representing a Drip Shield Component With a Contact Angle of 15°. Dimensions [1 in = 25.4 mm].

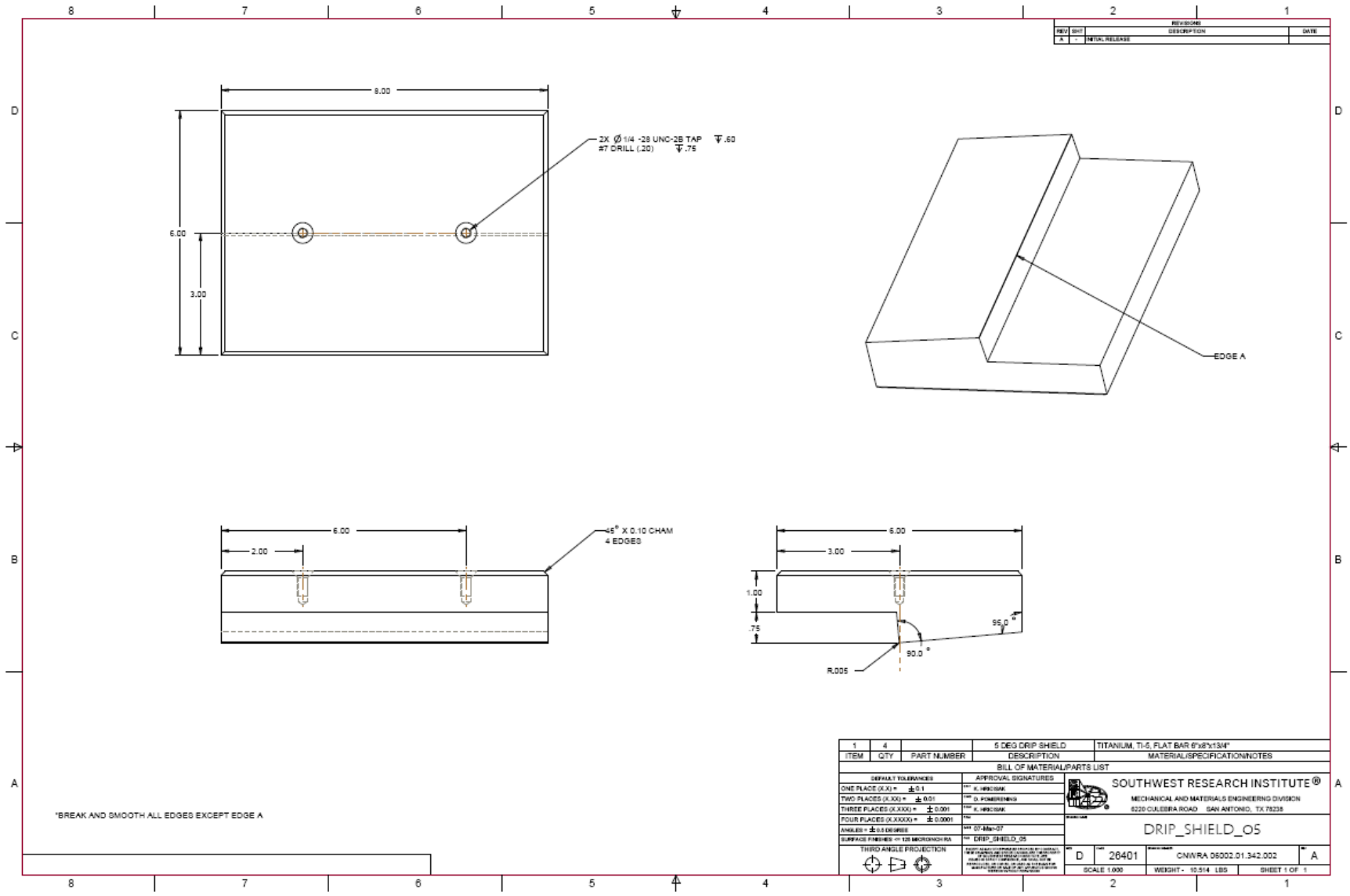

Figure 6. Titanium Grade 5 Plate Representing a Drip Shield Component With a Contact Angle of 5°. Dimensions [1 in = 25.4 mm].

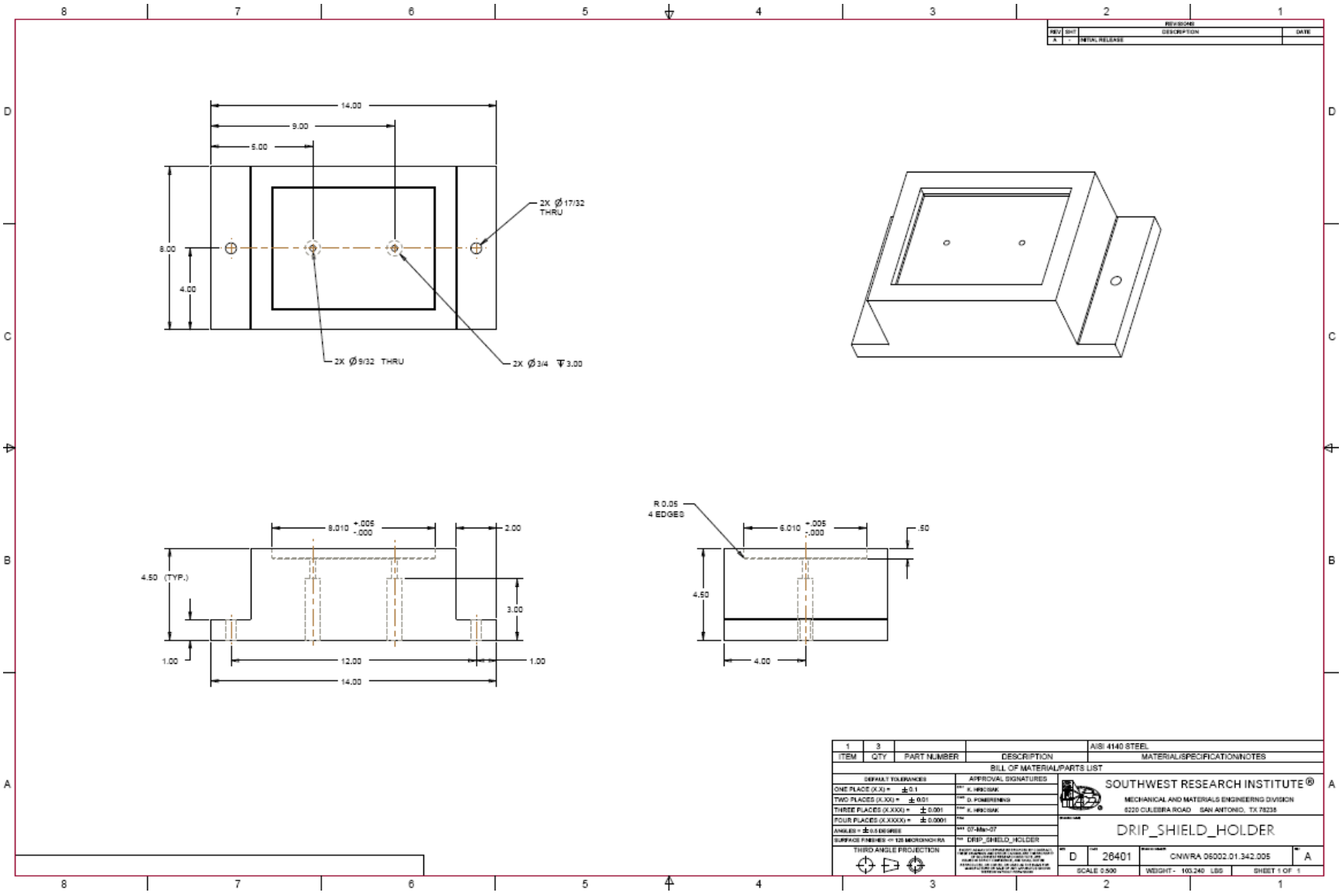

Figure 7. Steel Holder for Titanium Grade 5. Dimensions [1 in = 25.4 mm].

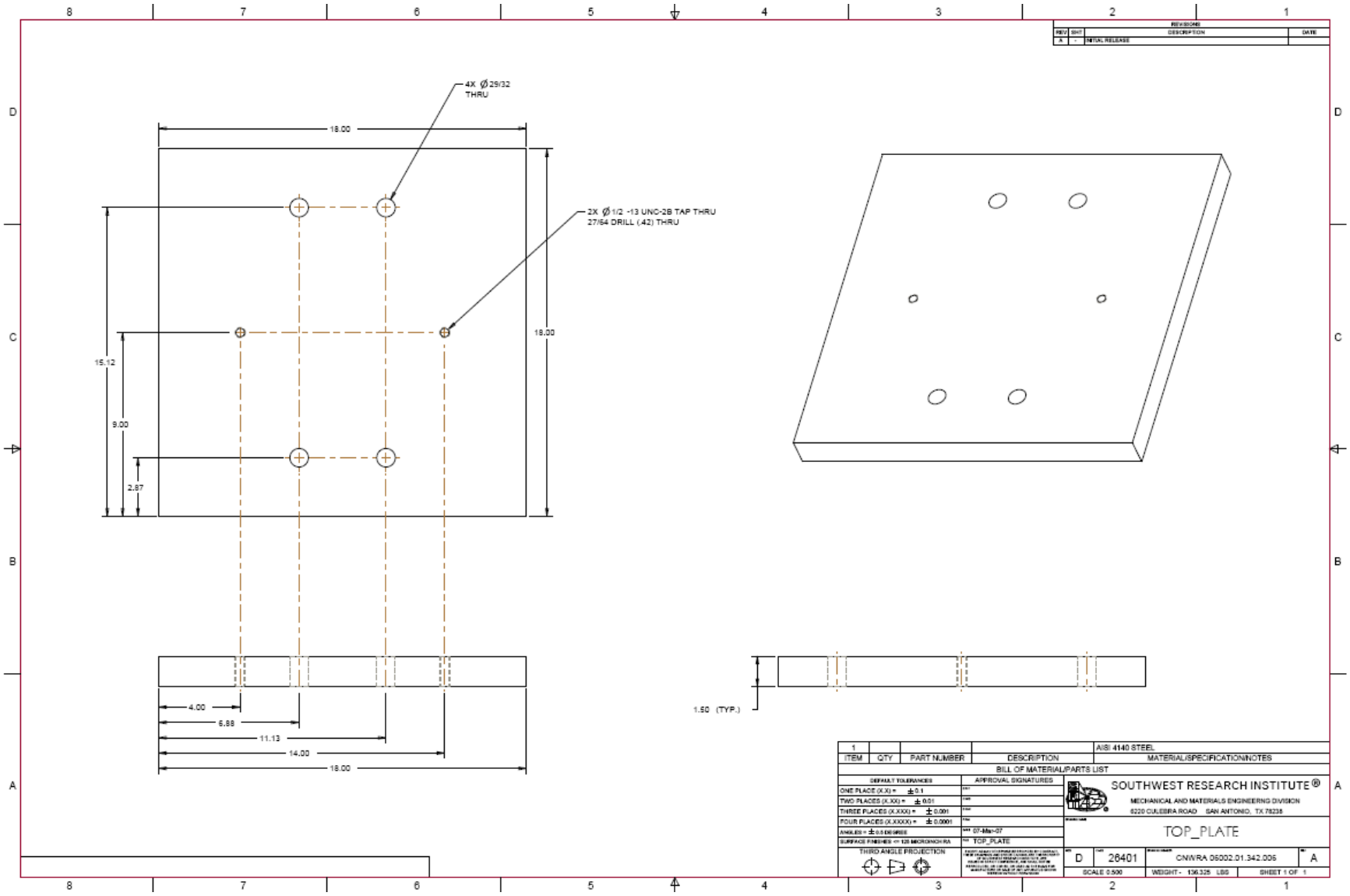

Figure 8. V-Top Steel Plate. Dimensions [1 in = 25.4 mm].